

# A hierarchical memory architecture overcomes context limits in long-horizon multi-agent computational modeling

Shivendra G. Tewari and Holly Kimko

Systems Medicine, Clinical Pharmacology & Safety Sciences, AstraZeneca, Gaithersburg, Maryland

## Abstract

Large language models (LLMs) demonstrate remarkable reasoning capabilities, yet their stateless architecture fundamentally limits deployment in long-horizon research workflows requiring multi-session continuity and quantitative rigor. Here we present *Ensemble QSP*, a multi-agent framework featuring a three-layer hierarchical memory architecture that keeps injected context bounded and constant in project duration (mid-term project state: median 301 tokens, max 4,050, across 104 runs) by capping each state category and evicting completed work, enabling continuous autonomous operation without context degradation. The system orchestrates five specialist worker agents under domain-expert principal investigators, enforcing physical constraints through physics-based checklists and structured-domain knowledge. Comprehensive benchmarking demonstrates robust autonomous pharmacokinetic-pharmacodynamic model selection without human intervention, consistent result quality across both lower-cost and frontier LLMs, improved PK parameter recovery relative to single-agent baselines, and stable model selection across linguistically diverse prompts of the same task. Feature-level ablation across physiologically based pharmacokinetic (PBPK) models spanning a broad complexity range shows that PI-agent oversight improves debugging efficiency while preserving final accuracy across conditions. The architecture is structurally domain-agnostic, adding a new scientific domain requires only a new PI agent configuration.

## Introduction

### *The context window bottleneck*

Large language models (LLMs) have advanced from text generation tools to scientific reasoning engines capable of autonomous chemical synthesis [1], protein structure prediction [2], and end-to-end scientific discovery and its publication [3]. These successes demonstrate sufficient parametric knowledge and reasoning capacity for complex scientific tasks. However, a critical gap persists, real scientific projects are not single-prompt endeavors. They unfold over weeks or months, require multi-session continuity, accumulate intermediate results, and demand adherence to domain-specific physical constraints throughout.

Quantitative systems pharmacology (QSP) exemplifies this challenge [4]. A typical QSP modeling workflow involves formulating systems of stiff ordinary differential equations (ODEs),

fitting parameters to heterogeneous non-clinical and clinical data from multiple studies, validating against held-out observations, and iterating across drug candidates at the same time maintaining physiological plausibility, unit consistency, and regulatory-grade documentation. No existing LLM agent framework supports such workflows autonomously, because they were designed for task-level completion rather than project-level continuity.

Multi-agent system (MAS) frameworks such as AutoGen [5], CrewAI, and LangChain-LangGraph enable role-based agent collaboration but treat context management naively: agents either pass full conversation histories (leading to  $O(N \times T)$  token growth where  $N$  is session count and  $T$  is tokens per session) or start fresh on each interaction (losing accumulated scientific knowledge). The AI Scientist [3] demonstrated end-to-end drug discovery followed by its paper generation but operates within a single session on well-scoped machine learning tasks, without addressing the stiff-ODE solving, multi-source data integration, and physical constraint enforcement that characterize mathematical biology.

We address this limitation with a hierarchical memory architecture comprising three bounded layers. The short-term layer holds the live working context injected each turn: a fixed window of recent conversation turns (4–20, set by model context size), a capped working-memory scratchpad ( $\leq 20,000$  characters for specialist agents,  $\leq 8,000$  for principal investigators) in which an agent records exact facts, file structure, parameter indices, data columns, so they survive context truncation, and a rolling buffer of the five most recent cross-agent task outcomes. The mid-term layer is a structured project-state JSON from which only bounded, task-relevant slices are injected: the five most-recent active user request's (with a running total), the 20 most-recently modified files, recent jobs, milestones, and the last three session summaries. This is paired with a separate auto-summarizing decision log (capped at 16,000 characters) that records why each step was taken. The long-term layer is project-independent domain knowledge: a  $\sim 24,000$ -character QSP modeling handbook injected into every specialist agent, per-domain knowledge files and physics checklists, and retrieval of source-paper text and reference code during code review. Because every layer is explicitly capped and completed work is evicted, the injected mid-term state stays bounded as a project runs across sessions, estimated median of 301 tokens (interquartile range 215–478; maximum 4,050) across 104 project runs, rather than growing with the full conversation history, which was unbounded in early prototypes. This replaces the  $O(N \times T)$  growth of naive history concatenation with context that is constant with respect to project duration.

## Results

### *System architecture*

The Ensemble QSP architecture addresses the context budget problem through structured state compression (Fig. 1). Instead of naively concatenating conversation history, which rapidly degrades LLM reasoning performance [6], the system maintains a categorized state (tasks, files created, issues encountered, jobs submitted, milestones achieved) with selective injection of only task-relevant fields. Decision logs are auto summarized, and domain knowledge is injected only when physics validation is triggered. This compresses a typical large-token project history into a compact-token structured state, preventing context window bloat over long-horizon projects.

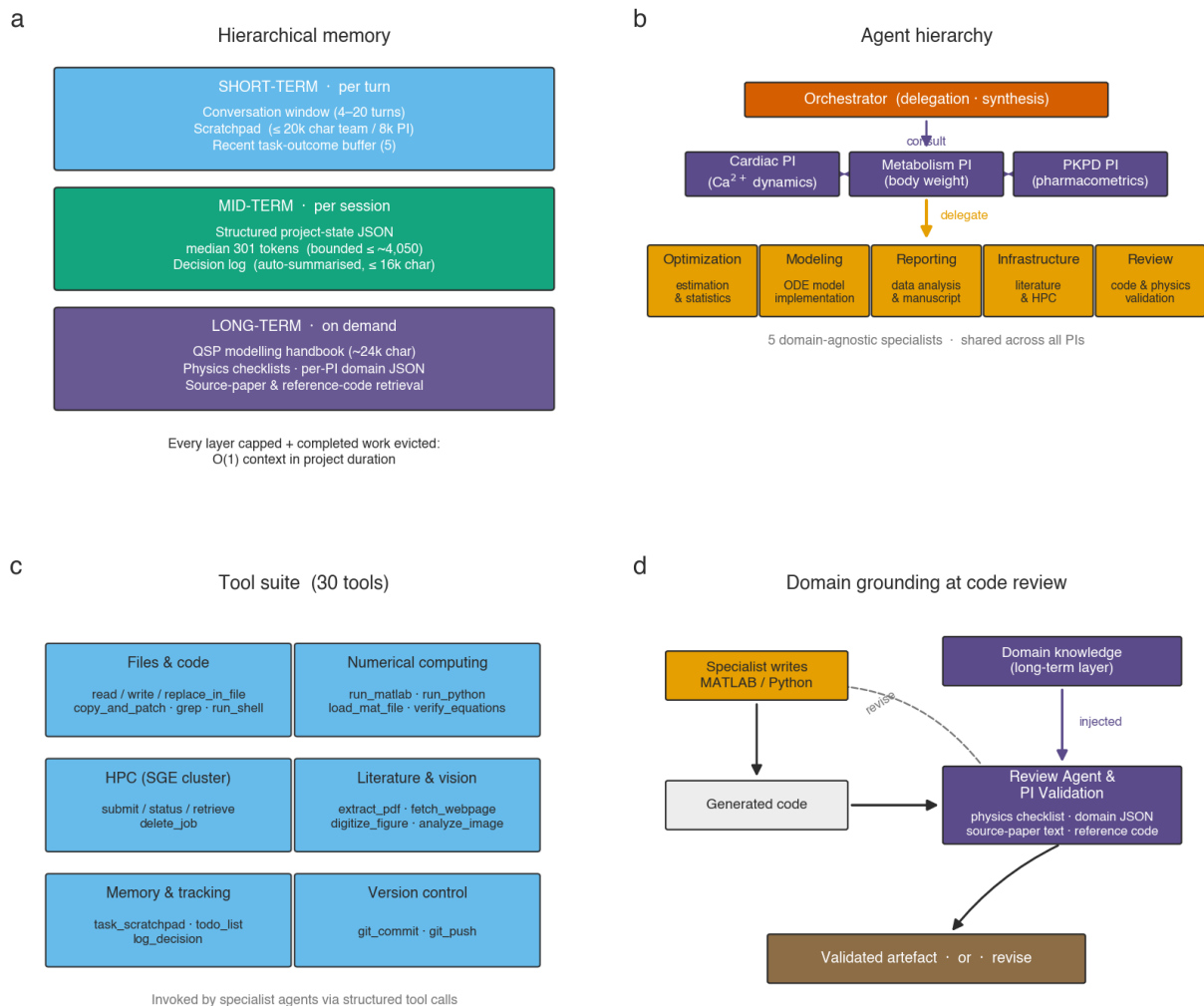


**Figure 1 | System architecture.** **a** Three-layer hierarchical memory: short-term working context (bounded conversation window plus a capped scratchpad, updated per turn), mid-term structured project state (JSON; median 301 tokens, updated per session), and long-term domain knowledge (handbook, physics checklists, and source-paper retrieval, on demand). **b** Agent hierarchy: the PI agent delegates to five specialist sub-agents with non-overlapping functional roles (optimization, modeling, reporting, infrastructure, and code review). **c** Tool suite spanning literature retrieval, numerical computing, HPC, and reporting. **d** Domain grounding: physics checklists, domain JSON, and RAG from publications are injected during code review and validation stages.

A two-tier agent hierarchy organizes computation and enables auto-looping of assigned tasks [7]. Any domain-expert principal investigator (PI) agents can be configured to provide strategic oversight. In this paper, we present three PI examples in metabolic physiology (energy balance and body weight change) and cardiac electrophysiology (calcium dynamics) to illustrate autonomous QSP parameter fitting, while PKPD modeling is used to benchmark multi-agent vs. single-agent systems. Five specialist sub-agents handle distinct, non-overlapping technical responsibilities: an Optimization Agent (parameter optimization and statistical analysis), a

Modeling Agent (mathematical modeling and ODE implementation), a Reporting Agent (data analysis and report writing), an Infrastructure Agent (literature search and HPC coordination), and a Review Agent (code quality reviewer). A central orchestrator manages delegation parsing, tool execution, consultation mechanisms, and result synthesis with parallel execution via thread pooling.

Domain grounding prevents the hallucination of physically implausible results [8, 9] through three mechanisms. First, physics checklists, i.e., domain-specific validation protocols (13 checks for cardiac calcium, 8 for energy balance, 8 for PKPD), are automatically injected during code review. Second, domain knowledge files encode model physiology, unit conventions, parameter ranges, and documented pitfalls in structured JSON formats. Third, retrieval augmented generation (RAG) [10] from indexed project publications enables a direct comparison between generated equations and published source material during the PI and Review Agent’s verification step.

The architecture is structurally domain-agnostic: specialist agents perform optimization, ODE implementation, analysis, literature search, and code review regardless of scientific domain. Adding a new domain requires only a new PI agent configuration (system prompt, domain JSON, and physics checklist). As evidence of this modularity, the three exemplary PI agents share identical sub-agent teams and a central orchestrator; adding a PI Agent (e.g., PKPD) required less than one day of development time with zero orchestrator changes. The `BasePIAgent` class handles all LLM provider logic, while domain-specific subclasses override only the necessary routing methods.

### *Multi-agent versus single-agent benchmarking*

We evaluated the system against a single-pass LLM baseline (GitHub Copilot, “GHCP”) across two complementary benchmarks with known ground truth (Fig. 2).

**PKPD model selection benchmark.** Twenty synthetic datasets were generated from six candidate model structures:  $2 \text{ PK} \times 3 \text{ PD}$ : one-compartment and two-compartment pharmacokinetics, each paired with  $E_{\max}$ , sigmoidal  $E_{\max}$ , and indirect response (IDR) pharmacodynamics. The multi-agent system achieved 100% correct model selection (20/20 datasets) on the first attempt with zero human intervention, whereas GHCP achieved 70% accuracy (14/20) but required nine human-assisted iterations/loops to self-identify the best ODE solver for the PKPD task, resulting in total  $9 \times 20$  (180 fitting scripts) versus 1 job (20 fits) for the MAS.

Performance differentiation was most pronounced on IDR datasets, which require solving stiff ODEs with appropriate initial conditions. The MAS correctly identified the structure, i.e., PK and PD model type, of all eight IDR datasets (100%) with a median PD parameter error of 14.1%, whereas GHCP identified only five (62%) with a median error of 68.4% on those correctly selected. For the simpler  $E_{\max}$  models, both systems performed comparably (MAS: 8.3% median error; GHCP: 5.0%), however, note that GHCP’s lower median error reflects 100-fold tighter solver tolerances perhaps adopted during its nine debugging iterations so not an equivalent comparison.

**PK parameter recovery benchmark.** Twenty difficult two-compartment subcutaneous PK profiles identified from 100,000 synthetic PK datasets were fitted under three conditions. The MAS recovered parameters within 10% of ground truth for 70% of profiles (14/20), compared with 20% for GHCP. Total wall-clock time was longer for the MAS (105 minutes versus 18–25 minutes), reflecting the overhead of multi-agent coordination. As a result of longer computing time, the number of successful ground-truth parameter value recoveries for GHCP are higher than MAS, but total number of ground truth recoveries are higher for MAS.

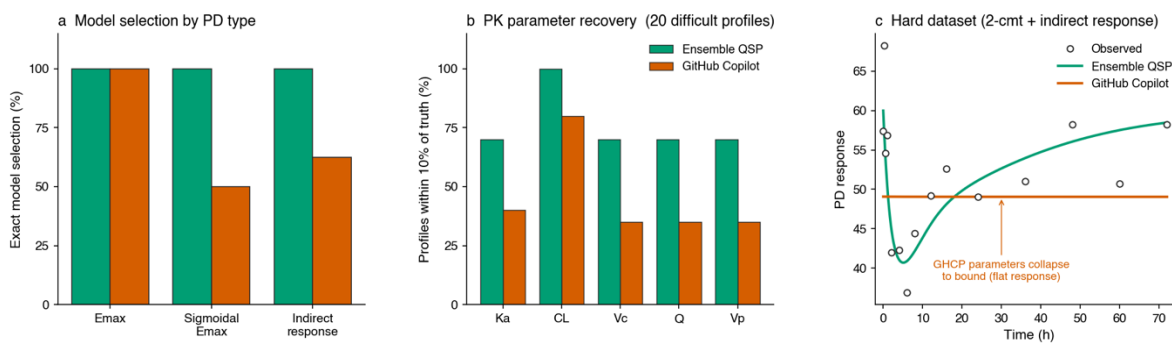


**Figure 2 | Multi-agent versus single-agent benchmarking.** **a** PKPD model selection accuracy across 20 synthetic datasets, stratified by PD model type: E<sub>max</sub>, sigmoidal E<sub>max</sub>, indirect response (IDR). MAS achieves 100% on first attempt; GHCP requires nine (self-debugging) iterations. **b** PK parameter recovery: fraction of profiles within 10% of ground truth with MAS and GHCP. **c** Representative fitted profiles for a difficult IDR dataset showing MAS simulation (green), GHCP simulation (orange), and data (open circles). Note that GHCP’s estimated IDR parameters ( $k_{in}$ ,  $k_{out}$ ,  $I_{max}$ ) stayed near their lower bounds, collapsing both the drug-driven perturbation term and the relaxation rate ( $k_{out}$ ), so the PD stayed near its baseline steady state, producing the flat line.

**A low-cost code-writer matches a frontier writer under full scaffolding.** A central question for practical deployment is whether the architecture’s accuracy depends on a frontier-scale code-writing agent, or whether the surrounding scaffolding, i.e., structured tools, domain knowledge, code review, and PI oversight, can elevate a substantially cheaper writer to the same task. We compared two configurations on a hard subset of 11 PKPD data (the indirect-response and two-compartment models that most stress model selection) from the PKPD benchmark, holding the architecture fixed and varying only the Optimization Agent’s backing model: a frontier writer (Claude 4.6 Opus, \$5/\$25 per million input/output tokens) versus a low-cost writer (Gemini 2.5 Flash, \$0.30/\$2.50).

Both configurations retained a frontier PI Agent (Gemini 3.1 Pro) and, where triggered, a mid-tier Review Agent (Claude 4.5 Sonnet). The low-cost writer matched the frontier writer on *both* axes: 11/11 correct PK and 11/11 correct PD structures (11/11 exact model selection) under each configuration, with statistically indistinguishable parameter recovery (Flash mean error 16.8%, median 6.8% across 77 parameters; Opus mean error 16.5%, median 6.8%). Accuracy was therefore invariant to writer-model scale, but only with the full scaffolding engaged. The code-review and PI-oversight loops repaired the low-cost writer’s coding errors (e.g., malformed file edits and data-alignment mistakes) that would otherwise have derailed the fits, with the PI Agent

supplying a corrective specification that recovered a dataset on which the cheaper writer initially stalled.

**Table 1 | Token usage and cost: low-cost vs. frontier code-writer**

Agent (role)	Model	Input token	Output token	Calls	Cost (\$)
<i>Low-cost writer: 11/11 exact, mean param error 16.8%</i>					
Optimization Agent (Writer)	Gemini 2.5 Flash	10,061,137	38,056	172	3.11
Review Agent (Review)	Claude 4.5 Sonnet	455,781	20,729	6	1.68
PI Agent (oversight)	Gemini 3.1 Pro	156,782	2,480	10	0.34
<b>Subtotal</b>		<b>10,673,700</b>	<b>61,265</b>	<b>188</b>	<b>5.14</b>
<i>Frontier writer: 11/11 exact, mean param error 16.5%</i>					
Optimization Agent (Writer)	Claude 4.6 Opus	1,845,982	42,751	32	10.30
PI Agent (oversight)	Gemini 3.1 Pro	97,167	1,240	5	0.21
<b>Subtotal</b>		<b>1,943,149</b>	<b>43,991</b>	<b>37</b>	<b>10.51*</b>

\*Review Agent usage was not recorded in the frontier run’s state, so its cost is a lower bound.

The cost structure reveals the trade-off precisely (Table 1). The low-cost-writer run was completed for \$5.14 (\$0.47 per dataset) versus \$10.51 (\$0.96 per dataset) for the frontier writer. Notably, this cost saving is far less than the per-token price difference between the two writer models, because the low-cost writer consumed 5.5-fold more input tokens (10.7M versus 1.9M): PI-directed and self-correction iterations, each re-reading files and prior context, erode most of the substantial per-token cost advantage. The result demonstrates that quality review, domain grounding, and PI-directed auto-looping let an inexpensive model perform a complex modeling task at frontier-equivalent accuracy and roughly half the cost. This means that the framework is not restricted to frontier models for these PKPD modeling tasks.

### *PI Agent oversight contribution at low and high complexity*

The PKPD benchmark above demonstrates the value of PI-directed autoloops at a fixed (PKPD) task complexity. To investigate whether PI Agent also matters for the frontier model as task complexity grows, we asked the system to implement MATLAB<sup>®</sup> codes of published mathematical models at opposite ends of an order-of-magnitude complexity range (i.e., a minimal atenolol model and a whole-body monoclonal-antibody model), both reproduced autonomously from their source PDFs. Because PDF-to-implementation fidelity is a supporting capability rather than the architectural claim of this work, the model reproduction pipeline is detailed in Supplementary Note S1. Figure 3 serves as the assessment of system’s architecture.

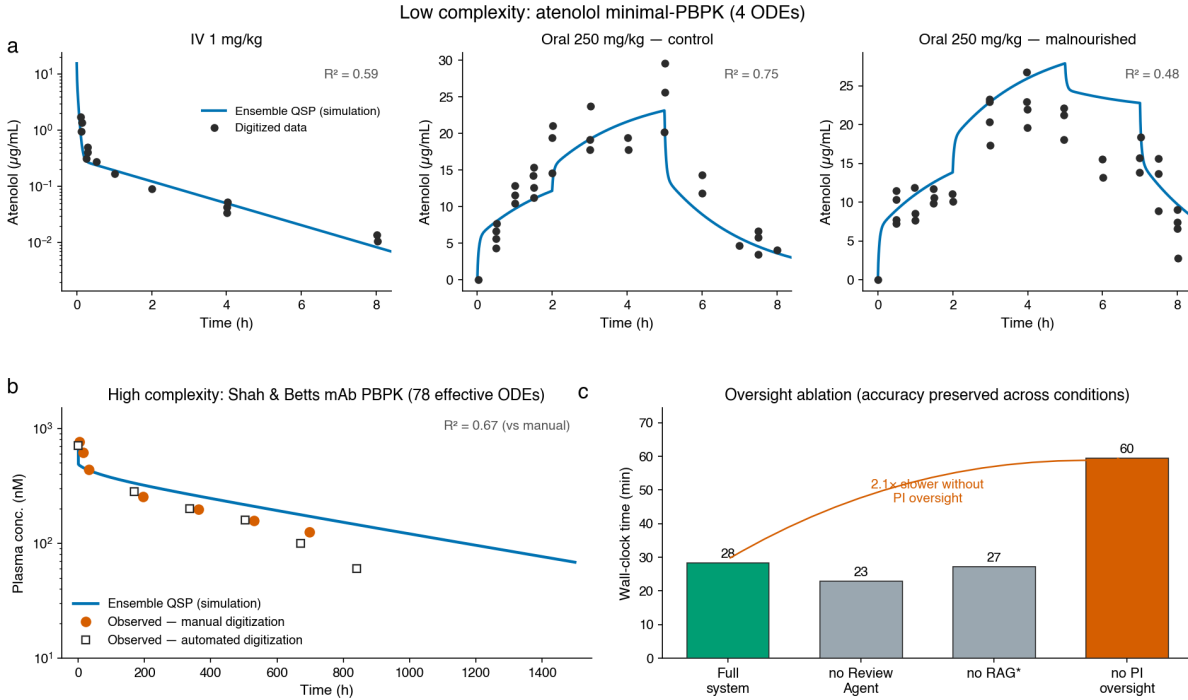


**Figure 3 | Autonomous model reproduction fidelity across complexity, and the value of PI oversight.** **a** Low complexity: autonomous reproduction of the atenolol minimal-PBPK model (4 ODEs; [11]). Ensemble QSP simulation (lines) plotted over manually digitized Figure-4 data (closed circles) for three scenarios (IV 1 mg/kg; oral 250 mg/kg control; oral 250 mg/kg malnourished). **b** High complexity: autonomous reproduction of the Shah & Betts [12] whole-body monoclonal-antibody PBPK model. Ensemble QSP simulation plotted over manual and automated digitization of Figure 8c (human IgG1, 5 mg/kg IV). Note that the LLM vision struggles to annotate data points accurately as it progresses further along the x-axis (square vs circle markers). The system implemented model used 78 effective ODEs, reproducing the published 93-state system via algebraic FcRn conservation rather than separate FcRn differential states; a mathematically equivalent, computationally efficient formulation derived autonomously. **c** Feature ablation on the 78-ODE model: final reproduction accuracy is preserved across conditions, but removing PI Agent model-physics oversight roughly doubles wall-clock time.  $R^2$  values are computed against manual digitization.

**Low complexity: atenolol minimal-PBPK (4 ODEs).** The full system reproduced the Kir et al. [11] model and recovered their published Figure-4 profiles across all three scenarios: intravenous ( $R^2 = 0.59$ ), oral control ( $R^2 = 0.75$ ), and oral malnourished ( $R^2 = 0.48$ ), see Fig. 3a. At this complexity, the task is tractable for the architecture as a whole; none of the tested architectural component are decisive when using a frontier model like Gemini 2.5 Pro or Claude 4.6 Opus.

**High complexity: monoclonal-antibody PBPK (93 ODEs).** The full system reproduced the Shah & Betts [12] whole-body monoclonal antibody (mAb) model directly from the source PDF, achieving  $R^2 = 0.67$  against manually digitized Figure-8c data (Fig. 3b). Notably, the implementation uses 78 effective ODEs, reproducing the published 93-state system by treating FcRn binding as an algebraic conservation constraint rather than separate differential states that are used in the paper; a mathematically equivalent, computationally efficient formulation that the system derived autonomously.

During reproduction, the system also autonomously detected a mass-conservation inconsistency in the published human parameter table of the Shah & Betts [12]: the tabulated lung plasma flow exceeded the summed peripheral-tissue flows it must balance. This discrepancy leaks antibody from the circulatory loop and artifactually shortens the predicted terminal half-life. The system diagnosed this via PI Agent’s mass-balance audit and imposed a flow-balancing constraint to restore conservation, recovering the characteristic FcRn-mediated long half-life.

Feature ablation at this scale showed that final accuracy was preserved across the tested ablation conditions, but removing the PI Agent’s model-physics oversight roughly doubled wall-clock time (2.1; from 28 min to 60 min; Fig. 3c). With the PI Agent oversight, the system received the balancing constraint directly and converged quickly, whereas without it, the system reached an equivalent conserving correction only after repeated unsuccessful attempts.

### *Linguistic invariance and prompt robustness*

Autonomous deployment requires that system behavior depends on the scientific content of a request, not on its surface phrasing. In the system architecture, we have handled this by enriching a user request with project memory layer and normalization of the user request by the PI Agent. To evaluate the impact of the PI Agent normalization on a user query, we tested two distinct properties of the PI normalization layer on a single benchmark task with known ground truth (see Supplementary Note: two-compartment PK with  $E_{\max}$  PD).

**Linguistic invariance** Does differential framing of an unambiguous task matter? We issued the same, fully specified modeling task through nine linguistically diverse rephrasing: terse imperative, formal British, casual American, ungrammatical non-native, bullet points, stream-of-consciousness, mixed-language (code-switching), passive academic, and emoji/Slack register, while holding the scientific request constant. The system achieved exact model selection in all nine variants (9/9, 100%), with a mean parameter-recovery error of 12.9% (median 13.4%, range 3.5–15.3%). Performance was therefore invariant to writing style, register, grammaticality, and language mixing: the PI layer abstracts surface linguistic variation into a single standardized technical specification (see Supplementary Note).

**Prompt robustness** Does specificity of an ambiguous task matter? A complementary test varied not the phrasing but the completeness of the task specification across eight prompts, ranging from a 519-character expert brief to a 134-character bare instruction. Six of eight (6/8) yielded exact model selection with a mean parameter error of 7.3% (median 3.5%). The two non-matching prompts, i.e., a deliberately vague junior-researcher request and a minimal 134-character instruction did not constitute system failures, since they lack an explicit specification of which PKPD structure needs to be fit; for these prompts, the system selected a simpler model (e.g. a one-compartment fit) rather than inventing requirements that were never stated. This is the desired behavior for an autonomous scientific agent: faithful execution of what was asked, without hallucinating unstated scope. Together, the two tests show the architecture is robust to how a well-posed task is phrased (linguistic invariance) while remaining appropriately sensitive to what is specified (prompt robustness); see Supplementary Note.

## *Literature pipeline benchmarking*

A critical prerequisite for autonomous modeling is the ability to locate, extract, and synthesize information accurately from scientific literature without human curation. We evaluated the end-to-end literature pipeline across retrieval, extraction, and synthesis using 17 test cases spanning cardiac electrophysiology, metabolic regulation, and PKPD (Table 2).

**Retrieval.** Ten queries (R01–R10) targeted known published papers across diverse modeling domains (population PK [13–15], PBPK, indirect-response PD [16], tumor growth inhibition [17], bone remodeling QSP [18, 19], and clinical trial reports [20–26]). On the first pass, the system correctly retrieved the specific targets for 7/10 queries (70% accuracy). The three target-misses (R02: Peterson & Riggs denosumab/RANKL model; R06: STEP/SURMOUNT trial papers; R09: SUSTAIN-1 primary paper) shared a common retrieval mode: topic-specified but not author-anchored queries retrieved thematically adjacent, but not the specific target papers. Reformulation of the three (R02, R06, and R09) queries to be author grounded recovered all three targets, achieving 10/10 (100%) post-optimization. Mean wall-clock time per query was 299 s (range 107–688 s); see Supplementary Note.

**Extraction with hallucination resistance.** Five cases (E01–E05) tested structured model-detail extraction from paper text, incorporating three adversarial “trap” cases designed to elicit hallucination. In E01, the target PMID was genuinely unretrievable (HTTP 404); the system reported “no records found” rather than fabricating model details. In E02 and E04, the supplied PMIDs pointed to irrelevant papers (an in-vitro molecular biology study [27] and a silkworm gene study [28], respectively); the system correctly classified both as off-domain and declined to extract modeling content. For the two genuine modeling papers (E03: Shah & Betts platform mAb PBPK [12]; E05: Dayneka et al. [16] indirect-response models), in this task, the system was fed an incorrect PMID but all other publication details were correct, the system extracted correct structural detail including compartment counts, mechanisms, and model families. Notably, the system detected the incorrect PMID mismatch, autonomously located the correct paper, and extracted its four indirect-response model structures. All five cases were adjudicated as correct by the PI Agent (5/5 behavioral pass). Mean wall-clock time was 175 s (range 90–436 s); see Supplementary Note.

**Multi-paper synthesis.** Two synthesis scenarios tested the most demanding tier of the pipeline: retrieving multiple related papers and reconciling quantitative findings into comparative artifacts. In S01 (semaglutide SC/IV versus oral population PK [14, 15]), the system retrieved and cross-referenced two Overgaard models, isolating absorption-pathway differences: absolute bioavailability  $\sim 0.7\text{--}0.8\%$  oral versus  $84.7\%$  subcutaneous, absorption rate  $K_a = 2.09\text{ h}^{-1}$  oral versus  $0.0253\text{ h}^{-1}$  SC, with apparent CL/F correctly inflated for the oral route. In S02 (mAb PBPK models with FcRn recycling), the system compiled a three-model comparison table (Shah & Betts [12], Li et al. [29], Hu et al. [30]) over compartmental structure, ODE count, and predicted human IgG1 half-life and flagged which ODE counts were author-reported versus inferred from equations, demonstrating calibrated confidence which is part of the system design. Both syntheses were verified by the PI Agent. Mean wall-clock time was 942 s, reflecting the multi-paper, multi-step nature of the synthesis task; see Supplementary Note.

**Table 2 | Literature pipeline benchmark results**

Tier	Cases (n)	Result	Traps	Mean time (s)
Retrieval (first pass) *	10	7/10 (70%)	N.A.	299
Retrieval (second pass)	10	10/10 (100%)	N.A.	–
Extraction (model-detail)	5	5/5 correct	3/5 (all passed)	175
Synthesis (multi-paper)	2	2/2 Manually verified	N.A.	942

\*Retrieved articles successfully matched the provided topic parameters but did not contain the specific target authors; refinement using author-anchored queries resulted in 100% specific target retrieval (second pass).

## *Autonomous QSP parameter fitting*

### Body-weight management case

We applied the full system to autonomous body-weight modeling for GLP-1 receptor agonist (GLP-1RA) drugs using the Hall 2024 body-composition QSP framework [31]. To simulate GLP-1RA effects, we added two receptor-occupancy functions: appetite suppression (reducing caloric intake) and homeostatic feedback attenuation (modulating the counter-regulatory response to weight loss via  $k_{prop}$ ). The system, when prompted, retrieved trial publications via optimized PubMed queries, extracted body-weight-time data from published figures using vision-language models, autonomously configured the PK model with trial-specific dose-escalation schedules, estimated pharmacodynamic parameters using the Hall model, and validated fits against observed clinical endpoints for three compounds (semaglutide, liraglutide, dulaglutide), progressing one at a time.

**Empirical dose-specific semaglutide data fitting.** In a first autonomous analysis phase, the system independently estimated four PD parameters:  $E_{\max, \text{GLP,app}}$  (maximum appetite suppression),  $EC_{\text{GLP,app}}$  (concentration at 50% of maximum appetite,  $EC_{50}$ ),  $E_{\max, k_{prop}}$  (maximum feedback suppression), and  $EC_{k_{prop}}$  (feedback  $EC_{50}$ ), at each of the seven semaglutide dose levels (0.5–16 mg) across five trial programs (SUSTAIN-1, SUSTAIN-7, SUSTAIN-FORTE, STEP-UP T2D, and PIONEER PLUS; 11 cohorts total). Since the system was not provided a PK model, the system autonomously retrieved semaglutide prescribing information from the FDA database and implemented a standard analytical one-compartment PK representation that is easily extendable to other compounds with available FDA labels. This approach directly utilized the FDA-reported terminal half-life and steady-state exposure proportionality, ensuring fidelity to established clinical exposures without the need for *de novo* structural model fitting. Based on the user’s request, the system also validated their one-compartment PK implementation with the published two-compartment model of Overgaard et al. [15], see Supplementary Note.

As expected, dose-specific fits achieved an RMSE < 0.85% body weight change across all 11 cohorts, with the lowest residuals at high doses (RMSE = 0.10–0.11% at 7.2–16 mg) and the highest at 1.0 mg (RMSE = 0.63–0.84%), reflecting inter-trial heterogeneity at this dose level. The system identified two key parameter trends:  $E_{\max, \text{GLP,app}}$  increased from 0.28 at 0.5 mg to 0.49 at 16 mg, suggesting a dose-dependent efficacy ceiling empirically; and  $EC_{\text{GLP,app}}$  converged to the lower bound (~100 pmol/L free) at low doses, indicating near-maximal receptor

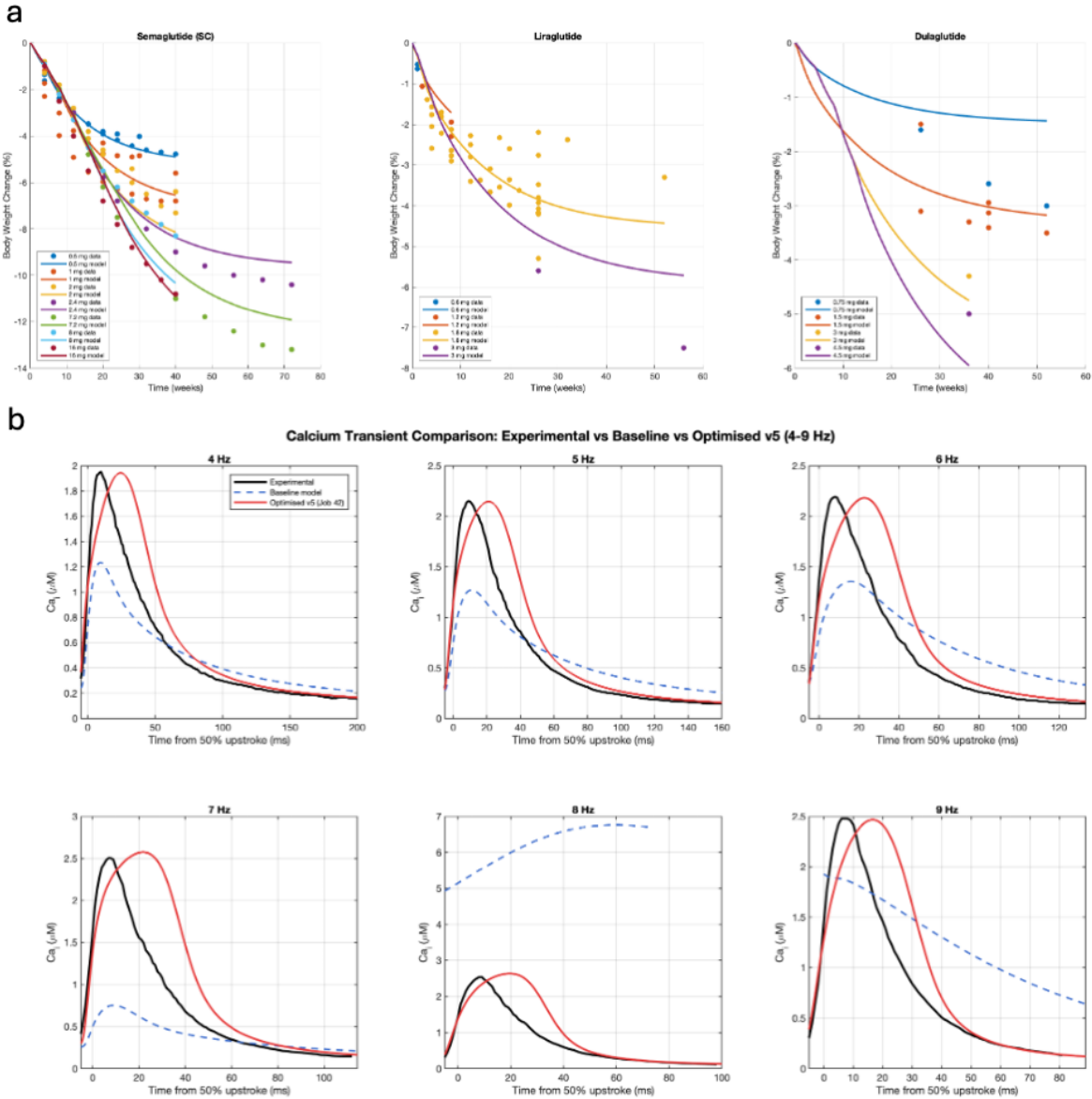


**Figure 4 | Autonomous model identification and parameter fitting.** **a** Hall model [31] coupled with drug-specific PK models. Model-predicted (lines) versus observed (symbols) percentage body weight change for semaglutide (blue, 11 cohorts, 0.5–16 mg), liraglutide (orange, 8 cohorts, 0.6–3.0 mg), and dulaglutide (green, 11 cohorts, 0.75–4.5 mg) from the combined 5-parameter fit. Each cohort was initialized by their representative body weight, height, and sex distribution. **b** Gattoni et al. [32] cardiac electrophysiology model. The system iteratively formulated and tested structural modifications to the baseline model to explain the frequency-dependent acceleration of relaxation (FDAR) observed in isolated rat ventricular myocytes. Model-predicted intracellular calcium transients for the baseline (dashed lines) and the optimized CaMKII-coupled variant (red lines) are compared against experimental recordings (black lines) across pacing frequencies from 4 to 9 Hz. The identified model successfully captures both the positive amplitude staircase and the accelerated decay kinetics at higher pacing rates.

occupancy.  $EC_{k_{prop}}$  varied over two orders of magnitude (2,500–200,000 pmol/L), which the system correctly flagged as poorly identifiable. During a subsequent domain-expert review, this lack of identifiability is likely driven by the relatively short duration of many included trials,

whereas the homeostatic feedback effect ( $k_{prop}$ ) primarily manifests in the extended time course required to reach a weight-loss plateau.

**Autonomous parameter estimation.** Based on dose-specific insights, the system autonomously designed and executed a combined 5-parameter fit across three structurally distinct GLP-1RAs (Fig. 4a): semaglutide (11 cohorts, 0.5–16 mg), liraglutide (8 cohorts, 0.6–3.0 mg), and dulaglutide (11 cohorts, 0.75–4.5 mg). The parameterization comprised drug-specific appetite  $EC_{50}$  values and shared GLP1-efficacy parameters ( $E_{max,app}$ ,  $EC_{k_{prop}}$ ), with  $E_{max,k_{prop}}$  fixed at 0.5 based on the sensitivity analysis and literature [31]. Parameter estimation used `particleswarm` and converged to the following  $EC_{GLP,app}$  values: 222 pmol/L (semaglutide), 616 pmol/L (liraglutide), 3888 pmol/L (dulaglutide), and shared  $E_{max,app}$  and  $EC_{k_{prop}}$  values of 0.384 and 1000 pmol/L (at lower bound), respectively. The resulting  $EC_{50}$  ranking on a free-concentration basis (semaglutide < liraglutide < dulaglutide) correctly recapitulates known clinical potency ordering.

## Cardiac electrophysiology case

**Autonomous model mechanism extension.** To test whether the system could autonomously update a QSP model, we applied the MAS to a structurally distinct domain: the frequency-dependent acceleration of relaxation (FDAR) in rat ventricular myocytes. The system was given the Gattoni et al. [32] 19-state, 64-parameter rat ventricular myocyte model, validated at 6 Hz, together with experimental calcium-transient features (amplitude, time-to-peak, and 50%/90% relaxation times;  $TD_{50}$ ,  $TD_{90}$ ) across pacing frequencies of 4–9 Hz.

The experimental data [33] exhibit a positive  $Ca^{2+}$  amplitude staircase, i.e., peak  $Ca^{2+}$  increasing from 1.81 to 2.43  $\mu$ M, and pronounced FDAR, i.e.,  $TD_{90}$  shortening from 82.5 ms at 4 Hz to 43.1 ms at 9 Hz. The baseline model reproduces neither behavior and becomes numerically unstable above its validated frequency of 6 Hz, predicting non-physiological relaxation prolongation ( $TD_{90} > 240$  ms at 9 Hz) and fails to relax at frequencies greater than 6 Hz (Fig. 4b).

Rather than treating the 64 parameters as fixed, the system serially hypothesized, implemented, and tested structural additions to the model, drawing on the cardiac electrophysiology literature to identify candidate frequency-sensing mechanisms. The system converged on a CaMKII-dependent regulatory module: active CaMKII—a frequency-dependent integrator of the calcium signal—accelerates SR calcium re-uptake by up-regulating SERCA activity through a Hill-type activation function, complemented by refinements to ryanodine-receptor release. This extended the model from 64 to 70 parameters and introduced biophysical coupling absent from the baseline formulation, providing a candidate mechanistic basis for FDAR in which faster pacing elevates CaMKII activity, which in turn speeds relaxation.

Fitting the extended model with `particleswarm` reproduced both the amplitude staircase and FDAR across all six frequencies, tracking peak  $Ca^{2+}$  increase from 1.80 to 2.52  $\mu$ M (simulated) and the near-halving of  $TD_{90}$  from 79.7 to 34.8 ms (simulated); fit quality was highest at lower frequencies and degraded modestly at the upper end of the range (0.13–0.15 at 8–9 Hz). Notably, parameters were estimated independently at each frequency rather than as a single shared set; the resulting frequency-dependent parameter shifts, concentrated in the CaMKII-SERCA pathway,

provide direct evidence for the proposed relaxation mechanism. A unified parameterization, in which one parameter set adapts to pacing rate through the CaMKII feedback loop itself, is an ongoing extension of this work.

## Discussion

The results demonstrate that hierarchical memory management, rather than model scale or prompting technique, is the primary enabler of long-horizon autonomous scientific computation with LLMs. The controlled ablation across a complexity gradient provides quantitative evidence that different architectural components address distinct failure modes at different scales, refuting the hypothesis that a single mechanism (e.g., better prompts) suffices.

**Complexity-dependent component value.** The PBP complexity range points to a scale-dependent role for architectural components: at low complexity (4 ODEs) the task is tractable for the architecture as a whole and no single component is decisive, whereas at high complexity (93 ODEs) PI Agent's strategic oversight roughly halves wall-clock time by preventing inefficient debugging of subtle inter-equation inconsistencies. Future work isolating the specific contribution of domain-knowledge retrieval at various scales will further sharpen this picture.

**Architectural versus model-capability contributions.** Two complementary tests isolate the PI Agent's normalization layer's role. Linguistic invariance (9/9 exact across nine paraphrasing of an identical task) shows performance is attributable to architectural normalization rather than to sensitivity to surface phrasing; prompt robustness (6/8, mean parameter error 7.3% across matching variants) shows the system remains appropriately sensitive to task content. The two non-matching prompts were deliberately under-specified and produced correct optimization for the simpler model they did specify, indicating that the system avoids hallucinating unstated requirements; a desirable safety property in regulatory facing environments.

**Scientific reasoning in the GLP-1RA case study.** The clinical fitting results demonstrate capabilities beyond parameter optimization: the system retrieved supporting data (FDA label values), implemented an explicit one-compartment linearized PK model that is extendable to multiple compounds, and performed sensitivity analysis to estimate key parameters for disentangling GLP1 compounds effects on appetite suppression and homeostatic feedback. By fixing the GLP1's maximal effect on homeostatic feedback, the system was able to untangle the drug-specific effect on appetite suppression from GLP1RA's effect on homeostatic feedback control suppression during weight loss.

This multi-step reasoning chain, spanning literature retrieval, hypothesis generation, model revision, and validation, was executed with minimal human intervention across multiple sessions, enabled by the hierarchical memory architecture preserving the scientific rationale across context boundaries. Initiated in January 2026, this project is one of the longest running projects of this system, running continuous analysis testing multiple novel hypothesis, demonstrating that the hierarchical memory architecture supports long-term projects with no visible degradation in multi-agent performance. Despite spanning several months, the accumulated compressed project state of this project is ~4,000 tokens, which helps the system maintain robust operational continuity and mitigating context-window exhaustion that is observed in standard LLM frameworks.

**Comparison with existing frameworks.** AutoGen [5], CrewAI, and LangChain-LangGraph provide multi-agent orchestration but lack persistent project state and domain-specific grounding. The AI Scientist [3] demonstrates research automation but within single sessions on machine-learning tasks. ChemCrow [34] integrated chemistry tools with LLMs as a single-agent system, but lacked long-horizon cross-session continuity. To our knowledge, Ensemble QSP is the first system combining autonomous scientific implementation, cross-session hierarchical memory, and domain-expert grounding for multi-month projects validated on published mathematical models. The literature pipeline benchmark further differentiates the architecture: the 100% adversarial-trap resistance (3/3 cases where the system correctly refused to fabricate content from irrelevant or unretrievable papers) reflects the PI Agent oversight enforcing scientific integrity at the extraction stage; a property absent from single-agent retrieval-augmented systems that lack domain-expert adjudication.

**Limitations.** The system depends on commercial LLM providers, introducing reproducibility concerns as models are updated; we mitigate this by logging all model versions. The domain grounding layer requires expert curation of physics checklists—a one-time investment per domain. Validation is currently confined to pharmacology, though the modular architecture (demonstrated by the addition of three PI Agent domains with zero orchestrator changes) provides structural evidence of generalizability. The GHCP comparison, while informative, reflects a single competing approach; broader comparisons with AutoGen and CrewAI on identical tasks were not feasible due to access and configuration constraints.

**Implications.** The demonstrated ability to autonomously reproduce published models and to fit clinical data across 30 cohorts and three drug classes with minimal human intervention suggests a near-term role for memory-augmented agent systems as computational research assistant. Compared to traditional workflows utilizing specialized pharmacometrics commercial software, which typically require 7 to 10 days of manual effort for preparing a PKPD report, the system can achieve similar quality results and reports in a few hours. These results demonstrate that the architecture does not replace domain experts but rather compresses timelines from weeks to days or hours for routine modeling tasks while maintaining scientific rigor through automated validation.

## Methods

**Language models.** The benchmark configuration used Gemini 3.1 Pro for the Principal-Investigator (PI) agents; Claude 4.6 Opus for the Optimization, Modeling, and Reporting agents; Claude 4.5 Sonnet for the Review agent; and GPT-5.5 for HPC coordination and literature retrieval (Infrastructure Agent). The provider and model for each agent are independently configurable; the cost-efficiency comparison (Table 1) additionally substituted Gemini 2.5 Flash for the Optimization Agent. All model versions and API parameters are logged per session to ensure reproducibility and audit.

**Agent orchestration.** The multi-agent system is implemented in Python 3.11+ with `concurrent.futures.ThreadPoolExecutor` for parallel agent execution. Agent communication follows a structured message protocol with typed fields. The PI Agent’s delegation logic routes tasks based on type, complexity, and required domain knowledge. Three autonomy levels

(Interactive, Semi-Autonomous, Autonomous) govern escalation conditions. All benchmark tests were performed using the ‘Autonomous’ mode.

**Ablation study design.** Eight architectural features are independently togglable via Boolean configuration flags in the `AblationConfig` data class. PKPD benchmark: A group of eleven difficult PKPD datasets, evaluated on model selection accuracy and parameter recovery. PBPK benchmarks: two published models of increasing complexity (Kir et al. [11], 4 ODEs; Shah & Betts [12], 93 ODEs), reproduced from PDF under ablation conditions. Metrics:  $R^2$  against manually digitized published data,  $C_{\max}$  error, half-life error, wall-clock time, and code volume.

**PKPD model-selection benchmark.** Twenty datasets with known ground truth were generated from six model structures (one- and two-compartment intravenous-bolus PK, each paired with direct  $E_{\max}$ , sigmoidal  $E_{\max}$ , or indirect-response Type IV PD). All profiles used a 100 mg IV bolus dose sampled at 15 time points spanning 0–72 h (0, 0.25, 0.5, 1, 2, 4, 6, 8, 12, 16, 24, 36, 48, 60, 72 h). Ground-truth parameters were fixed per dataset (not randomly sampled) across the ranges:  $CL$ : 0.5–4.5 L/h;  $V_c$ : 5–25 L;  $Q$ : 0.3–2.5 L/h (two-compartment structures only);  $V_p$ : 8–30 L (two-compartment only);  $E_{\max}$ : 70–200;  $EC_{50}$ : 1.0–8.0;  $\gamma$ : 1.5–3.5 (sigmoidal  $E_{\max}$  only);  $k_{in}$ : 6–20;  $k_{out}$ : 0.05–0.4  $h^{-1}$ ;  $I_{\max}$ : 2–10;  $IC_{50}$ : 1.0–8.0 (indirect-response only). Synthetic PK and PD observations each included 10% proportional residual error (multiplicative Gaussian noise on the noise-free simulated trajectory).

**PK parameter-recovery benchmark.** A separate pool of 100,000 synthetic two-compartment subcutaneous PK profiles was generated to probe parameter identifiability independently of model-selection difficulty. Each profile simulated a single 1 mg SC dose with dense hourly sampling over a 336 h (14-day) horizon; the five governing parameters ( $K_a$ ,  $CL$ ,  $V_c$ ,  $Q$ ,  $V_p$ ) were drawn independently per profile by log-uniform sampling over ranges representative of a large-molecule SC biologic ( $K_a$ : 0.005–0.200  $h^{-1}$ ;  $CL$ : 0.005–0.250 L/h;  $V_c$ : 1.0–15.0 L;  $Q$ : 0.01–3.0 L/h;  $V_p$ : 1.0–20.0 L). From an initial multi-start fitting pass on the first 100 of the 100,000 profiles, each profile was graded by its worst single-parameter percentage error (across  $K_a$ ,  $CL$ ,  $V_c$ ,  $Q$ ,  $V_p$ ; A: <1%, B: <5%, C: <25%, D: <100%, F:  $\geq$ 100%) and classified by failure mode:  $K_a$ – $V_c$  swap,  $Q$ – $V_p$  non-identifiability, or convergence to a spurious local minimum. The 20 profiles graded D or F, the most severe identifiability failures, were retained as the hard-profile subset reported in the PK parameter-recovery results (Fig. 2b).

**Linguistic invariance and prompt robustness design.** Two complementary prompt-sets both targeted the same benchmark PKPD task with known ground truth (Dataset 11 of the PKPD dataset). For *linguistic invariance*, the identical, fully specified task was rephrased into nine linguistically diverse variants (terse imperative, formal British, casual American, ungrammatical non-native, bullet points, stream-of-consciousness, mixed-language/code-switching, passive academic, and emoji/Slack register), holding scientific content constant. For *prompt robustness*, eight variants instead varied the completeness/specificity of the task (519-character expert brief down to a 134-character bare instruction). Success was defined as exact model selection match; parameter-recovery error is reported for matching variants. Both prompt-sets are single-replicate ( $n = 9$  and  $n = 8$ ). Model-selection scoring uses functional equivalence (e.g. “2cmt”, “2-compartment” and “two\_compartment” are treated as the same structure).

**Literature retrieval benchmark.** Ten queries spanning cardiac electrophysiology, metabolic regulation, and PKPD were tested against known target papers. For queries that initially failed to

retrieve the target publication due to overly generic search terms, the search was systematically refined. This refinement involved anchoring the queries with specific author names to appropriately narrow the search space, followed by re-evaluation and final manual verification of the results which (as expected) succeeded after including authors of the targeted papers in the queries.

**GLP-1RA clinical data sources and digitization.** Semaglutide, liraglutide, and dulaglutide body-weight-time data were either digitized from published figures or obtained from CODEx<sup>®</sup> database. Automated figure digitization uses vision-language models (Claude 4.5 Sonnet) with structured validation against reported summary statistics by the Review Agent. Pharmacokinetic parameters ( $C_{ss}$ ,  $t_{1/2}$ ) were sourced from FDA prescribing information and published population PK analyses.

**Body weight QSP model.** The Hall body-composition model [31] comprises a 6-state ODE system (adaptive thermogenesis, glycogen, fat mass, lean mass, extracellular water, linear trend). GLP-1RA pharmacodynamic effects enter via two occupancy functions operating on free drug concentration: (1) appetite suppression:  $\text{Intake}(t) = \text{appetite\_factor} \times \text{Intake}_{\text{init}} - k_{\text{prop,eff}} \times (\text{BW}(t) - \text{BW}_{\text{init}})$ , where the appetite factor is modulated by receptor occupancy  $\text{occ}_{\text{app}} = c_{\text{free}} / (EC_{\text{GLP,app}} + c_{\text{free}})$ ; and (2) homeostatic feedback attenuation via an analogous  $k_{\text{prop}}$  occupancy function. Dose-escalation PK was modeled as piecewise exponential approach to steady state with trial-specific titration schedules.

**Ventricular myocyte calcium model.** The baseline model was the Gattoni et al. [32] 19-state, 64-parameter rat ventricular myocyte ODE system, which couples action potential generation with calcium cycling across the cytosol and sarcoplasmic reticulum (SR), including dynamic buffering by troponin, and which is validated at 1 Hz and 6 Hz. Experimental calcium-transient features (peak amplitude, TTP,  $TD_{50}$ , and  $TD_{90}$ ) were extracted for each of the six pacing frequencies (4–9 Hz) and fitted with particleswarm; parameters were estimated independently at each frequency rather than as a single shared set. A unified parameterization in which one parameter set adapts to pacing rate through the CaMKII feedback loop is an ongoing extension of this work.

**Simulation environment.** Parameter estimation jobs are submitted to a Sun Grid Engine managed cluster via automated job submission and retrieval, performed by the Infrastructure Agent. The ablation study used fixed data seeds with varying LLM seeds across conditions. All ODE systems are solved in MATLAB<sup>®</sup> R2025b. The ode solvers, tolerances, and optimization functions were chosen by the system depending on the modeling task as described in the `modeling_handbook.py`.

**Code availability.** The complete Ensemble QSP platform, including user prompts, agent prompts, domain knowledge files, physics checklists, benchmark datasets, ablation harness, and prompt robustness variants, is available at [repository URL].

**Data availability.** All pre-clinical and clinical trial data used in this study are derived from published sources cited in the reference list or was obtained from the CODEx<sup>®</sup> database from Certara. Synthetic benchmark datasets and results, digitized clinical data, fitted parameters, and performed benchmark tests are deposited at [repository URL].

## Acknowledgments

We gratefully acknowledge Dr. Kevin D. Hall for his conceptual guidance regarding the disentanglement of appetite suppression and homeostatic feedback mechanisms in the GLP-1RA QSP analysis. We also gratefully acknowledge Prof. James Zou for his valuable feedback on the manuscript.

## Competing Interests

SGT and HK are employees of AstraZeneca and hold shares/share options in AstraZeneca.

## References

1. Boiko, D.A., et al., *Autonomous chemical research with large language models*. Nature, 2023. **624**(7992): p. 570-578.
2. Lin, Z., et al., *Evolutionary-scale prediction of atomic-level protein structure with a language model*. Science, 2023. **379**(6637): p. 1123-1130.
3. Lu, C., et al., *The ai scientist: Towards fully automated open-ended scientific discovery*. arXiv preprint arXiv:2408.06292, 2024.
4. Azer, K. and J.S. Barrett, *Quantitative system pharmacology as a legitimate approach to examine extrapolation strategies used to support pediatric drug development*. CPT Pharmacometrics Syst Pharmacol, 2022. **11**(7): p. 797-804.
5. Wu, Q., et al., *Autogen: Enabling next-gen llm applications via multi-agent conversation*. arXiv preprint arXiv:2308.08155, 2023.
6. Liu, N.F., et al., *Lost in the middle: How language models use long contexts*. Transactions of the association for computational linguistics, 2024. **12**: p. 157-173.
7. Hong, S., et al. *MetaGPT: Meta programming for a multi-agent collaborative framework*. in *International Conference on Learning Representations*. 2024.
8. Poweleit, E.A., A.A. Vinks, and T. Mizuno, *Artificial Intelligence and Machine Learning Approaches to Facilitate Therapeutic Drug Management and Model-Informed Precision Dosing*. Ther Drug Monit, 2023. **45**(2): p. 143-150.
9. McKenna, N., et al. *Sources of hallucination by large language models on inference tasks*. in *Findings of the association for computational linguistics: EMNLP 2023*. 2023.
10. Lewis, P., et al., *Retrieval-augmented generation for knowledge-intensive nlp tasks*. Advances in neural information processing systems, 2020. **33**: p. 9459-9474.
11. Kir, F., S. Sahin, and W.J. Jusko, *Minimal Physiologically-Based Pharmacokinetic Modeling of Atenolol and Metoprolol Absorption in Malnourished Rats*. Eur J Drug Metab Pharmacokinet, 2025. **50**(3): p. 251-263.
12. Shah, D.K. and A.M. Betts, *Towards a platform PBPK model to characterize the plasma and tissue disposition of monoclonal antibodies in preclinical species and human*. J Pharmacokinet Pharmacodyn, 2012. **39**(1): p. 67-86.
13. Yang, X.D. and Y.Y. Yang, *Clinical Pharmacokinetics of Semaglutide: A Systematic Review*. Drug Des Devel Ther, 2024. **18**: p. 2555-2570.

14. Overgaard, R.V., et al., *Clinical Pharmacokinetics of Oral Semaglutide: Analyses of Data from Clinical Pharmacology Trials*. Clin Pharmacokinet, 2021. **60**(10): p. 1335-1348.
15. Overgaard, R.V., et al., *Population Pharmacokinetics of Semaglutide for Type 2 Diabetes*. Diabetes Ther, 2019. **10**(2): p. 649-662.
16. Dayneka, N.L., V. Garg, and W.J. Jusko, *Comparison of four basic models of indirect pharmacodynamic responses*. J Pharmacokinet Biopharm, 1993. **21**(4): p. 457-78.
17. Simeoni, M., et al., *Predictive pharmacokinetic-pharmacodynamic modeling of tumor growth kinetics in xenograft models after administration of anticancer agents*. Cancer Res, 2004. **64**(3): p. 1094-101.
18. Peterson, M.C. and M.M. Riggs, *Predicting nonlinear changes in bone mineral density over time using a multiscale systems pharmacology model*. CPT Pharmacometrics Syst Pharmacol, 2012. **1**(11): p. e14.
19. Peterson, M.C. and M.M. Riggs, *A physiologically based mathematical model of integrated calcium homeostasis and bone remodeling*. Bone, 2010. **46**(1): p. 49-63.
20. Overgaard, R.V., et al., *Liraglutide 3.0 mg for Weight Management: A Population Pharmacokinetic Analysis*. Clin Pharmacokinet, 2016. **55**(11): p. 1413-1422.
21. Wilding, J.P., et al., *Exposure-response analyses of liraglutide 3.0 mg for weight management*. Diabetes Obes Metab, 2016. **18**(5): p. 491-9.
22. Rubino, D.M., et al., *Effect of Weekly Subcutaneous Semaglutide vs Daily Liraglutide on Body Weight in Adults With Overweight or Obesity Without Diabetes: The STEP 8 Randomized Clinical Trial*. JAMA, 2022. **327**(2): p. 138-150.
23. Garvey, W.T., et al., *Two-year effects of semaglutide in adults with overweight or obesity: the STEP 5 trial*. Nat Med, 2022. **28**(10): p. 2083-2091.
24. Feng, P., et al., *A Phase 1 Multiple Dose Study of Tirzepatide in Chinese Patients with Type 2 Diabetes*. Adv Ther, 2023. **40**(8): p. 3434-3445.
25. Aronne, L.J., et al., *Continued Treatment With Tirzepatide for Maintenance of Weight Reduction in Adults With Obesity: The SURMOUNT-4 Randomized Clinical Trial*. JAMA, 2024. **331**(1): p. 38-48.
26. Nicze, M., et al., *Resistant and Refractory Obesity: The Complexity of Anti-Obesity Therapy Failure*. Int J Mol Sci, 2026. **27**(6).
27. Thompson, T., et al., *1,25-dihydroxyvitamin D3 enhances the apoptotic activity of MDM2 antagonist nutlin-3a in acute myeloid leukemia cells expressing wild-type p53*. Mol Cancer Ther, 2010. **9**(5): p. 1158-68.
28. Ye, W., et al., *Cloning and functional analysis of autophagy-related gene 7 in Bombyx mori, silkworm*. Arch Insect Biochem Physiol, 2021. **107**(4): p. e21827.
29. Li, L., et al., *Simulation of monoclonal antibody pharmacokinetics in humans using a minimal physiologically based model*. AAPS J, 2014. **16**(5): p. 1097-109.
30. Hu, S., A. Datta-Mannan, and D.Z. D'Argenio, *Physiologically Based Modeling to Predict Monoclonal Antibody Pharmacokinetics in Humans from in vitro Physiochemical Properties*. MAbs, 2022. **14**(1): p. 2056944.
31. Hall, K.D., *Physiology of the weight-loss plateau in response to diet restriction, GLP-1 receptor agonism, and bariatric surgery*. Obesity (Silver Spring), 2024. **32**(6): p. 1163-1168.
32. Gattoni, S., et al., *The calcium-frequency response in the rat ventricular myocyte: an experimental and modelling study*. J Physiol, 2016. **594**(15): p. 4193-224.

33. Janssen, P.M., L.B. Stull, and E. Marbán, *Myofilament properties comprise the rate-limiting step for cardiac relaxation at body temperature in the rat*. Am J Physiol Heart Circ Physiol, 2002. **282**(2): p. H499-507.
34. A, M.B., et al., *Augmenting large language models with chemistry tools*. Nat Mach Intell, 2024. **6**(5): p. 525-535.